Results in Engineering 26 (2025) 105305

Contents lists available at ScienceDirect

Results in Engineering

journal homepage: www.sciencedirect.com/journal/results-in-engineering

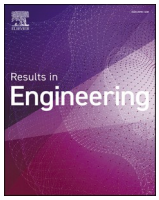

Analytical modelling of cillia- driven prandtle fluid flow in a horizontal tube with viscous dissipation using homotopy perturbation method

Saira Muhammad Hussain [a], Aqila Shaheen [a], Ali Hasan Ali [b,c,d,e,*], Ali Raza [f], Ahmed M. Abed [g,h]

[a] School of Mathematics, Minhaj University Lahore, Pakistan
[b] Department of Mathematics, College of Education for Pure Sciences, University of Basrah, Basrah, 61004, Iraq
[c] Institute of the Mathematics, University of Debrecen, Pf. 400, H-4002, Debrecen, Hungary
[d] Technical Engineering College, Al-Ayen University, Thi-Qar, 64001, Iraq
[e] Department of Business Management, Al-Imam University College, Balad, 34011, Iraq
[f] Department of Mathematics, University of Engineering and technology Lahore, Pakistan
[g] Department of the Industrial Engineering, College of Engineering, Prince Sattam Bin Abdulaziz University, Al Kharj, 16273, Saudi Arabia
[h] Industrial Engineering Department, Zagazig University, Zagazig, 44519, Egypt

ARTICLE INFO

Keywords:
Prandtle fluid
Cilia effect
Horizontal tube
Viscous dissipation
Homotopy perturbation method

ABSTRACT

This work analytically investigates the effects of viscous dissipation on cilia-induced Prandtl fluid flow in a horizontal tube. Approximate formulations for temperature and velocity profiles are obtained by solving the governing nonlinear equations using the Homotopy Perturbation Method (HPM). A comprehensive analysis is conducted on the influence of critical parameters such as the Prandtl number, viscosity ratio, and characteristics of ciliary motion. The impact of viscous dissipation on the thermal field is examined to understand its contribution to energy transfer. Graphs are employed to explore the effects of various stimulation parameters on heat and flow transfer. The structure of the equations is solved analytically, and graphical representations illustrate the pressure gradient, pressure rise, stream function, and velocity. Additionally, the analysis in ciliated tubes is effectively visualized through these graphs. The model enhances the realism of physiological and industrial transport simulations by emphasizing the significant effects of viscous dissipation on energy distribution and fluid velocity. A key innovation lies in incorporating viscous effects into a Prandtl fluid framework, which has often been neglected in previous studies. Near the tube walls, the fluid's peak temperature increases by approximately 15–25 % as ε rises (e.g., from 0.01 to 0.1). Thermal gradients become steeper and thermal boundary layers narrower at higher Prandtl numbers (e.g., from 5 to 20). The shear-thinning behavior becomes more pronounced as β increases (from 0.5 to 2.0), resulting in reduced effective viscosity. The graphical results validate HPM's accuracy and efficiency in modeling flow dynamics. With potential applications in biological systems such as the lungs and bile ducts, as well as in porous geological media, the findings offer valuable insights for applied mathematics and fluid mechanics.

1. Introduction

Fluid dynamics is one of the most attractive and fascinating scientific concepts, with implications in nearly every aspect of life. Numerous fields in construction and applied sciences including the food industry, power conversion devices, climatology, geology, bioengineering, and hydraulic control systems benefit from the study of fluid mechanics. Unlike Newtonian fluids, non-Newtonian fluids do not exhibit a linear relationship between shear stress and shear rate, making their behavior complex and dependent on the type of fluid and the conditions under which it flows. Peristaltic waves generate a pressure gradient that drives the fluid forward. This research proposal aims to conduct numerical simulations of non-Newtonian fluid flow in various geometries, with a focus on applications involving peristaltic motion and cilia-driven flows.

An analytical study was conducted on chemically reactive, nonlinear mixed convective magnetohydrodynamic (MHD) flow involving Joule heating and activation energy in Prandtl–Eyring nanofluids. The impact

* Correspondence author.
E-mail addresses: rayansultan765@gmail.com (S.M. Hussain), shaheenaqila@gmail.com (A. Shaheen), ali.hasan@science.unideb.hu (A.H. Ali), maleraxa@gmail.com (A. Raza), a.abed@psau.edu.sa (A.M. Abed).

https://doi.org/10.1016/j.rineng.2025.105305
Received 5 February 2025; Received in revised form 30 April 2025; Accepted 12 May 2025
Available online 13 May 2025

Nomenclature

$\vec{U}, \vec{W}$	Velocity profiles (m s^{-1})
$\vec{C}$	Concentration (kgm^{-3})
D_m	Mass diffusivity (m^2 s^{-1})
g	Gravitational acceleration (m s^{-2})
c_p	Specific heat (J/kg K)
T_m	Mean fluid temperature
$\overline{\overline{A_1}}$	First revilin Ericson tensor
B_r	Brinkman number
Sc	Schmidt number
Pr	Prandtl number
$\vec{P}$	Pressure (kgm^{-1}s^{-2})
$\vec{T}$	Temperature (K)
k	Thermal conductivity (W m^{-1} K^{-1})
Q_0	Heat absorption (W m^{-3}K^{-1})
Q	Heat absorption
k_T	Thermal diffusion ratio
G	Thermal Grashof number
S_r	Soret effect
M	Magnetic field

of square pin fins on heat transfer in a multi-mini-channel heat sink has been numerically assessed in various hydrothermal studies, as discussed by many researchers [1–6]. Amador et al. [7] explored the implications for memory and learning in the adult hippocampus, highlighting the role of motile cilia in driving the proliferation of amplifying progenitor cells. Bangs et al. [8] investigated the lineage specificity of primary cilia in mouse embryos. Fatima et al. [9] presented a case study on mass and heat transfer induced by ciliated tubes within a double layer of viscous fluid flow. Shaheen et al. [10] analyzed Non-Newtonian fluid flow in a symmetrical tube with ciliated walls using a metachronal wave model. In another study, Shaheen et al. [11] examined the application of nanoparticles in MHD flow of a tangent hyperbolic fluid through a ciliated fallopian tube. Khaderi et al. [12] investigated symmetry breaking in microfluidic propulsion driven by artificial cilia.

Conduction, convection, and radiation are the three primary mechanisms of heat transfer. Researchers also consider the mass transfer of various chemical species, whether hot or cold, to optimize thermal performance. Although these mechanisms possess distinct characteristics, they typically occur simultaneously within a system. The impact of partial slip on Sisko nanofluid double-diffusive convection in an asymmetric channel under an inclined magnetic field and peristaltic propulsion has been discussed in recent studies. Convection theory applied to asymmetric channels with partial slip and viscosity effects in thermally reactive peristaltic flow in a Prandtl-type tilted magneto-nanofluid has also been investigated [13–15].

Kazaz et al. [16] analyzed the performance of sensible heat thermal energy storage using both mono and blended nanofluids in an inclined system influenced by free convection and radiation. In another work, Kazaz et al. [17] emphasized the importance of the interaction between radiation and nanoparticles in improving light absorption and enhancing heat conversion efficiency. Ullah et al. [18] studied the heat and mass transfer of chemically reactive nanofluid flow over a stretched sheet in a magnetic field, noting significant effects from thermal density and viscous dissipation. Imran et al. [19] examined the peristaltic flow of Jeffrey six-constant nanofluids in vertically non-uniform tubes. Bhattacharyya et al. [20] reported on the use of hybrid magnetic nanofluids and magnetic field-assisted mini-channel cooling systems for solar PV panel applications.

Hybrid nanofluid versus nanofluid: This study investigates MHD flow and heat transfer at the stagnation point across a stretching or shrinking surface, considering partial slip and viscous dissipation. It explores heat transfer in an MHD stagnation-line flow modeled using a cross fluid formulation over a stretched surface. The study also examines the impact of changing thermal conductivity in ternary hybrid nanofluids over a stretching sheet, under the influence of a magnetic field and convective boundary conditions. Additionally, it analyzes Sisko fluid flow in a nanofluid thin film with variable heat transfer on an unsteady stretching surface in the presence of an external magnetic field.

Convective mass and heat transfer in a rotating cone with chemical reactions and internal heat generation within a magneto-Jeffrey fluid flow is also discussed. Various non-Newtonian properties are briefly outlined following the concept of non-Newtonian fluids [21–26]. Shaheen et al. [27] investigated the three-dimensional flow of nanofluids over an exponentially stretched nonlinear horizontal sheet saturated with a porous medium. Wakif et al. [28] proposed a novel computational method to simulate radiative Casson fluids in stable MHD convective flows, incorporating temperature-dependent viscosity and thermal conductivity over a horizontally stretched sheet with irregular geometry. Carter et al. [29] examined the maintenance of a multipotent progenitor phenotype in olfactory horizontal basal cells. Abuasbeh et al. [30] discussed entropy generation in MHD peristaltic flow through a symmetric curved horizontal channel for a non-Newtonian fluid. Amanullah et al. [31] presented a numerical analysis of Carreau non-Newtonian fluid flow past an isothermal sphere using magnetic field modeling. Recent advancements in mechanics have explored how thermal radiative biological flows of six-constant Jeffreys nanofluids interact with induced magnetic fields, double-diffusive convection, and multiple slip conditions [32], and several other related studies can be found in [33–38].

The governing equations are solved using a closed-form solution, and the effects of the Hartmann number (Ha), Prandtl number (Pr), Soret number (Sr), and Schmidt number (Sc) on velocity and temperature profiles are analyzed. The results indicate that increasing Ha significantly suppresses flow velocity due to the Lorentz force, while a higher β enhances fluid elasticity, leading to more pronounced flow variations. Moreover, an increase in Pr reduces thermal diffusion, resulting in a steeper temperature gradient, whereas a higher Sr enhances heat transfer at the boundary. The study also reveals that for $Ha = 2.0,\ \beta = 0.5,\ Pr = 5.0$ and $Sr = 0.2$, the maximum velocity decreases by 18 %, while the temperature at the boundary increases by 12 % compared to lower parameter values. These findings provide fundamental results into biological and industrial applications where cilia-driven transport plays a crucial role.

Ciliary motion refers to the movement of cilia hair-like structures on the surface of cells. Cilia play essential roles in various biological processes, such as clearing mucus in the respiratory tract or transporting eggs in the female reproductive system. Heat transfer in fluids containing suspended nanoparticles can be engineered to enhance the fluid's properties in ways that benefit ciliary motion. For example, enhancing heat transfer can alter the viscosity or thermal conductivity of the fluid, thereby affecting the efficiency of ciliary movement. This study also investigates the effects of forced fluid dissipation on the characteristics of heat transfer from a tube embedded in a horizontal plate maintained at a constant surface temperature. The analysis is conducted using cylindrical coordinates in two dimensions. Nonlinear partial differential equations, such as the velocity equation are solved using the Homotopy Perturbation Method (HPM), while the temperature and concentration equations are solved exactly. Graphical results are presented using MATLAB. Our findings demonstrate that HPM not only provides accurate results but also offers rapid convergence.

2. Problem Formulation

The incompressible peristaltic flow of nanofluids containing iron oxide nanoparticles in a uniform tube is described using cylindrical coordinates (R,Z), where Z represents the axial direction of the tube and

R denotes the radial direction (see Fig. 1). Two coordinate systems are used to describe this section: one moving at a constant speed and the other stationary.

The governing equations for continuity and nanoparticle concentration can be written as follows [8]:

$$\frac{\partial \vec{U}}{\partial \vec{R}}+\frac{\vec{U}}{\vec{R}}+\frac{\partial \vec{W}}{\partial \vec{Z}}=0 \tag{1}$$

$$\rho\left(\vec{U}\ \frac{\partial}{\partial \vec{R}}+\vec{W}\frac{\partial}{\partial \vec{Z}}+\frac{\partial}{\partial \vec{t}}\right)\vec{U}\ =-\frac{\partial \vec{P}}{\partial \vec{R}}+\frac{1}{\vec{R}}\frac{\partial}{\partial \vec{R}}\left(\vec{R}\vec{S}_{\vec{R}\vec{R}}\right)+\frac{\partial}{\partial \vec{Z}}\left(\vec{S}_{\vec{R}\vec{Z}}\right)-\frac{\vec{S}_{\vec{\theta}\vec{\theta}}}{\vec{R}} \tag{2}$$

$$\rho\left(\vec{U}\ \frac{\partial}{\partial \vec{R}}+\vec{W}\frac{\partial}{\partial \vec{Z}}+\frac{\partial}{\partial \vec{t}}\right)\vec{W}\ =-\frac{\partial \vec{P}}{\partial \vec{Z}}+\frac{1}{\vec{R}}\frac{\partial}{\partial \vec{R}}\left(\vec{R}\vec{S}_{\vec{R}\vec{Z}}\right)+\frac{\partial}{\partial \vec{Z}}\left(\vec{S}_{\vec{Z}\vec{Z}}\right)-\sigma B_0^2\vec{W} \tag{3}$$

$$\rho c_p\left(\vec{U}\ \frac{\partial}{\partial \vec{R}}+\vec{W}\frac{\partial}{\partial \vec{Z}}+\frac{\partial}{\partial \vec{t}}\right)\vec{T}\ =\vec{S}_{\vec{R}\vec{R}}\frac{\partial \vec{U}}{\partial \vec{R}}+\vec{S}_{\vec{R}\vec{Z}}\frac{\partial \vec{W}}{\partial \vec{R}}+\vec{S}_{\vec{R}\vec{Z}}\frac{\partial \vec{U}}{\partial \vec{Z}}+\vec{S}_{\vec{Z}\vec{Z}}\frac{\partial \vec{U}}{\partial \vec{R}}+\vec{S}_{\vec{\theta}\vec{\theta}}\frac{\vec{U}}{\vec{R}}$$

$$+\vec{K}\left(\frac{\partial^2\vec{T}}{\partial \vec{R}^2}+\frac{1}{\vec{R}}\frac{\partial \vec{T}}{\partial \vec{R}}+\frac{\partial^2\vec{T}}{\partial \vec{Z}^2}\right) \tag{4}$$

$$\left(\vec{U}\ \frac{\partial}{\partial \vec{R}}+\vec{W}\frac{\partial}{\partial \vec{Z}}+\frac{\partial}{\partial \vec{t}}\right)\vec{C}=D\left(\frac{\partial^2\vec{C}}{\partial \vec{R}^2}+\frac{1}{\vec{R}}\frac{\partial \vec{C}}{\partial \vec{R}}+\frac{\partial^2\vec{C}}{\partial \vec{Z}^2}\right)$$

$$+\frac{D\vec{K}_T}{\vec{T}_0}\left(\frac{\partial^2\vec{T}}{\partial \vec{R}^2}+\frac{1}{\vec{R}}\frac{\partial \vec{T}}{\partial \vec{R}}+\frac{\partial^2\vec{T}}{\partial \vec{Z}^2}\right) \tag{5}$$

Here, $\boldsymbol{P}$ denotes the pressure, and $\boldsymbol{U}$ and $\boldsymbol{W}$ are the velocity components in the axial ($\boldsymbol{Z}$) and radial ($\boldsymbol{R}$) directions, respectively, of the fixed reference frame. $\boldsymbol{T}$ is the temperature, ρ is the density, c_p is the specific heat at constant pressure, and k is the thermal conductivity.

$\boldsymbol{K}$ represents the coefficient of pseudoplasticity. The envelope of the cilia tips can be mathematically expressed as follows:

$$\vec{R}=\vec{H}=\vec{f}\left(\vec{Z},\ \vec{t}\right)=a+a\epsilon\cos\left(\frac{2\pi}{\lambda}\left(\vec{Z}-c\vec{t}\right)\right), \tag{6}$$

$$\vec{Z}=\vec{g}\left(\vec{Z},\ \vec{Z}_0,\ \vec{t}\right)=a+a\epsilon\alpha\sin\left(\frac{2\pi}{\lambda}\left(\vec{Z}-c\vec{t}\right)\right), \tag{7}$$

The radius of the ciliated tube corresponds to a wavelength characterized by the mean wave speed, a non-dimensional parameter related to the cilia, denoted by c. The elliptical motion of the cilia tips is quantified by the eccentricity, represented by α. The only velocities that convey the fluid are those induced by the motion of the cilia tips. Here, a denotes the mean radius of the tube, ϵ is a non-dimensional parameter representing cilia length, and λ and c represent the wavelength and speed of the metachronal wave, respectively. A measures the eccentricity of the elliptical motion, and $\boldsymbol{Z}_0$ indicates the reference position of a particle.

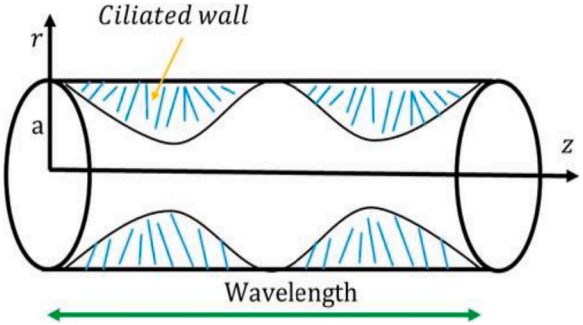

Fig. 1. Geometry of the problem.

Under the no-slip condition, the velocities of the moving fluid are solely those induced by the motion of the cilia tips, and are given by:

$$\vec{W}=\frac{\partial \vec{Z}}{\partial \vec{t}\vec{z}_0}=\frac{\partial \vec{g}}{\partial \vec{t}}+\frac{\partial \vec{g}}{\partial \vec{Z}}\frac{\partial \vec{Z}}{\partial \vec{t}}=\frac{\partial \vec{g}}{\partial \vec{t}}+\frac{\partial \vec{g}}{\partial \vec{Z}}\vec{W}, \tag{8}$$

$$\vec{U}=\frac{\partial \vec{R}}{\partial \vec{t}\vec{z}_0}=\frac{\partial \vec{f}}{\partial \vec{t}}+\frac{\partial \vec{f}}{\partial \vec{Z}}\frac{\partial \vec{Z}}{\partial \vec{t}}=\frac{\partial \vec{f}}{\partial \vec{t}}+\frac{\partial \vec{f}}{\partial \vec{Z}}\vec{W}, \tag{9}$$

By applying Eqs. (6) and 7 in Eqs. (8) and 9, we get:

$$\vec{W}=\frac{-\frac{2\pi}{\lambda}\left(\epsilon a\cos\left(\frac{2\pi}{\lambda}\right)\left(\vec{Z}-c\vec{t}\right)\right)}{1-\frac{2\pi}{\lambda}\left(\epsilon a\cos\left(\frac{2\pi}{\lambda}\right)\left(\vec{Z}-c\vec{t}\right)\right)},$$

$$\vec{U}=\frac{\frac{2\pi}{\lambda}\left(\epsilon a\sin\left(\frac{2\pi}{\lambda}\right)\left(\vec{Z}-c\vec{t}\right)\right)}{1-\frac{2\pi}{\lambda}\left(\epsilon a\cos\left(\frac{2\pi}{\lambda}\right)\left(\vec{Z}-c\vec{t}\right)\right)}$$

The two tubes' flow is unsteady in the given coordinates ($\vec{R},\ \vec{Z}$). Moving with the same velocity as a wave in the Z-direction, it fixes in a wave frame ($\vec{r},\ \vec{z}$). Between the two frames, the transformations are:

$$\vec{r}=\vec{R},\ \vec{z}=\vec{Z}-c\vec{t}\vec{u}=\vec{U},\ \vec{z}=\vec{W}-c_1$$

The corresponding boundary conditions are defined as:

$$\frac{\partial \vec{w}}{\partial \vec{r}}=0,\ \frac{\partial \vec{T}}{\partial \vec{R}}=0,\ \frac{\partial \vec{C}}{\partial \vec{R}}=0\ at\ \vec{R}=0$$

$$\vec{W}=0,\ K\frac{\partial \vec{T}}{\partial \vec{R}}=-\eta\left(\vec{T}-\vec{T}_0\right),\ \vec{C}=\vec{C}_o,\ at\ \vec{R}=\vec{H}=a+b\cos\left[\frac{2\pi}{\lambda}\left(\vec{Z}-c\vec{t}\right)\right]$$

The basic equation of the Prandtle fluid model is as below:

$$S_{rz}=\alpha\left(\frac{\partial w}{\partial r}\right)+\beta\left(\frac{\partial w}{\partial r}\right)^3$$

Dimensionless equations can be written as

$$\frac{\partial u}{\partial r}+\frac{u}{r}+\frac{\partial w}{\partial z}=0$$

$$\delta R_e\left(u\frac{\partial w}{\partial r}+w\frac{\partial w}{\partial z}\right)=-\frac{\partial P}{\partial z}+\frac{S_{rz}}{r}+\frac{\partial}{\partial r}S_{rz}+\delta\frac{\partial}{\partial z}(S_{zz})-M^2(w+1)$$

$$\delta\left(u\frac{\partial \theta}{\partial r}+w\frac{\partial \theta}{\partial z}\right)=\frac{1}{r}\left(\frac{\partial^2\theta}{\partial r^2}+\frac{1}{r}\frac{\partial \theta}{\partial r}+\delta^2\frac{\partial^2\theta}{\partial z^2}\right)+B_k\frac{\partial w}{\partial r}(rS_{rz})$$

$$\delta\left(u\frac{\partial \sigma}{\partial r}+w\frac{\partial \sigma}{\partial z}\right)=\frac{1}{S_c}\left(\frac{\partial^2\sigma}{\partial r^2}+\frac{1}{r}\frac{\partial \sigma}{\partial r}+\delta^2\frac{\partial^2\sigma}{\partial z^2}\right)+S_r\left(\frac{\partial^2\theta}{\partial r^2}+\frac{1}{r}\frac{\partial \theta}{\partial r}+\delta^2\frac{\partial^2\theta}{\partial z^2}\right)$$

Here the non-dimensional considered are as follows:

$$R=\frac{\vec{R}}{a},\ r=\frac{\vec{r}}{a},\ Z=\frac{\vec{Z}}{\lambda},\ z=\frac{\vec{z}}{\lambda},\ W=\frac{\vec{w}}{c},\ w=\frac{\vec{w}}{c},\ U=\frac{\lambda\vec{U}}{ac},\ u=\frac{\lambda\vec{u}}{ac},\ t=\frac{c_1\vec{t}}{\lambda},\ \lambda_1=\frac{\epsilon_1 c_1}{a},$$

$$\lambda_2=\frac{\epsilon_2 c_1}{a},\ R_e=\frac{ac_1\rho}{\mu_0},\ \delta=\frac{a}{\lambda},\ h=\frac{\vec{h}}{a}=1+\epsilon\cos(2\pi z),\ P_r=\frac{\mu_0 c_p}{k},\ G_r=\frac{g\alpha a_2^3\vec{T}_0}{\nu^2},$$

$$\theta = \frac{\left(\vec{T} - \vec{T}_0\right)}{\vec{T}_0}, \alpha = \frac{\kappa}{(\rho c)_f},\ p = \frac{a^2 \vec{p}}{c_1 \lambda \mu_0},\ S_c = \frac{\rho D \kappa_T \vec{T}_0}{\mu T_0 \vec{C}_0},\ S_r = \frac{\mu}{D_\rho},\ B_k = \frac{g \alpha a_2^3 \vec{C}_0}{\nu^2},$$

$$\sigma = \frac{\left(\vec{C} - \vec{C}_0\right)}{\vec{C}_0}, M = \sqrt{\frac{\sigma}{\mu}} B_0 a.$$

Non-inertial in terms of neglecting due a small Reynold number, which is $1>>R_e$ when $1>>\delta$ is a long-wavelength approximation. The flow in the fluid in a tube is very slow.

$$\frac{\partial u}{\partial r} + \frac{u}{r} + \frac{\partial w}{\partial z} = 0 \tag{10}$$

$$\frac{\partial P}{\partial r} = 0 \tag{11}$$

$$-\frac{\partial P}{\partial z} + \frac{1}{r}\frac{\partial}{\partial r}(\mathrm{rS_{rz}}) - M^2(w+1) = 0 \tag{12}$$

$$\frac{1}{r}\frac{\partial}{\partial r}\left(r\frac{\partial \theta}{\partial r}\right) + B_k \frac{\partial w}{\partial r}(\mathrm{rS_{rz}}) = 0 \tag{13}$$

$$\frac{1}{S_c}\left(\frac{1}{r}\frac{\partial}{\partial r}\left(r\frac{\partial \sigma}{\partial r}\right)\right) + S_r\left(\frac{1}{r}\frac{\partial}{\partial r}\left(r\frac{\partial \theta}{\partial r}\right)\right) = 0 \tag{14}$$

So above equations become

$$\frac{\partial P}{\partial r} = 0$$

$$\frac{\partial \mathrm{P}}{\partial \mathrm{z}} = \frac{1}{r}\frac{\partial}{\partial r}\left(r\left(\alpha\left(\frac{\partial \mathrm{w}}{\partial \mathrm{r}}\right) + \beta\left(\frac{\partial \mathrm{w}}{\partial \mathrm{r}}\right)^3\right)\right) + M^2(w+1) \tag{15}$$

$$\frac{1}{r}\frac{\partial}{\partial r}\left(r\frac{\partial \theta}{\partial r}\right) + B_k \frac{\partial w}{\partial r}\left(r\left(\alpha\left(\frac{\partial \mathrm{w}}{\partial \mathrm{r}}\right) + \beta\left(\frac{\partial \mathrm{w}}{\partial \mathrm{r}}\right)^3\right)\right) = 0 \tag{16}$$

$$\frac{1}{S_h}\left(\frac{1}{r}\frac{\partial}{\partial r}\left(r\frac{\partial \sigma}{\partial r}\right)\right) + S_T\left(\frac{1}{r}\frac{\partial}{\partial r}\left(r\frac{\partial \theta}{\partial r}\right)\right) = 0 \tag{17}$$

Boundary conditions are given below

$$\frac{\partial w}{\partial r} = 0,\ \frac{\partial \theta}{\partial r} = 0,\ \frac{\partial \sigma}{\partial r} = 0 \ at\ r = 0$$

$$w = -1 - 2\pi\epsilon\delta\gamma\cos(2\pi z),\ \frac{\partial \theta}{\partial r} + \kappa\theta = 0,\ \sigma = 0 \ at\ r = h = 1 + \epsilon\cos(2\pi z)$$

3. Solution of the problem

Exact Temperature and Concentration Solution

$$\frac{1}{r}\frac{\partial}{\partial r}\left(r\frac{\partial \theta}{\partial r}\right) = -B_k \frac{\partial w}{\partial r}\left(r\left(\alpha\left(\frac{\partial \mathrm{w}}{\partial \mathrm{r}}\right) + \beta\left(\frac{\partial \mathrm{w}}{\partial \mathrm{r}}\right)^3\right)\right) \tag{18}$$

$$\frac{1}{S_h}\left(\frac{1}{r}\frac{\partial}{\partial r}\left(r\frac{\partial \sigma}{\partial r}\right)\right) = -S_T\left(\frac{1}{r}\frac{\partial}{\partial r}\left(r\frac{\partial \theta}{\partial r}\right)\right) \tag{19}$$

3.1. Solution for the velocity profile

$$\frac{\partial \mathrm{P}}{\partial \mathrm{z}} = \frac{1}{r}\frac{\partial}{\partial r}(\mathrm{rS_{rz}}) + M^2(w+1)$$

$$\mathrm{S_{rz}} = \alpha\left(\frac{\partial \mathrm{w}}{\partial \mathrm{r}}\right) + \beta\left(\frac{\partial \mathrm{w}}{\partial \mathrm{r}}\right)^3$$

$$\frac{\partial \mathrm{P}}{\partial \mathrm{z}} = \frac{1}{r}\frac{\partial}{\partial r}\left(r\left(\alpha\left(\frac{\partial \mathrm{w}}{\partial \mathrm{r}}\right) + \beta\left(\frac{\partial \mathrm{w}}{\partial \mathrm{r}}\right)^3\right)\right) + M^2(w+1)$$

3.2. Homotopy Perturbation method for velocity profile

The combination of structural perturbation and homotopy analysis led to the development of the analytical and exact Homotopy Perturbation Method (HPM). The governing equations are solved using this method.

$$L(w) = L(w_{10}) - \mathrm{qL}(w_{10}) - q\left[\alpha\left(\frac{\partial w}{\partial r}\right)^n + \beta\left(\frac{\partial w}{\partial r}\right)^{n-1} - M^2(w+1) - \frac{\partial P}{\partial z}\right] \tag{20}$$

We select Linear operator $L = \frac{1}{r}\frac{\partial}{\partial r}\left(r\frac{\partial}{\partial r}\right)$ and initial guess that satisfy a required boundary conditions were

$$w_{10} = -1 - 2\pi\epsilon\delta\gamma\cos(2\pi z) + \left(\frac{r^2 - h^2}{4}\right)P_0$$

H (q, w) in shear-thinning fluid

$$\mathrm{H(q,w)} = L(w) - L(w_{10}) + \mathrm{qL}(w_{10}) + q[N(w) - f(r)]$$

$$\mathrm{H(q,w)} = L(w) - L(w_{10}) + \mathrm{qL}(w_{10}) + q\left[\frac{b}{r}\left(\frac{\partial w}{\partial r}\right)^2 + 2b\left(\frac{\partial w}{\partial r}\right)\left(\frac{\partial^2 w}{\partial r^2}\right) - M^2(w+1) - \frac{\partial P}{\partial z}\right]$$

According to HPM, we define

$w = w_0 + \mathrm{qw_1} + q^2 w_2 + \ldots\ldots\ldots\ldots$

$P = P_1 + \mathrm{qP_2} + q^2 P_3 + \ldots\ldots\ldots\ldots$

$$L(w_0 + qw_1 + \ldots\ldots) = L(w_{10}) - qL(w_{10}) - q\alpha\left[\left(\frac{\partial(w_0 + qw_1 + \ldots.)}{\partial r}\right)^2 + \beta\left(\frac{\partial(w_0 + qw_1 + \ldots.)}{\partial r}\right)^3 - M^2(w_0 + qw_1 + \ldots. + 1) - \frac{\partial(P_1 + qP_2 + \ldots.)}{\partial z}\right]$$

Zeroth Order:

$$L(w_0) = L(w_{10})$$

First Order:

$$L(w_1) = -L(w_{10}) - \alpha\left(\frac{\partial w_0}{\partial r}\right) - \beta\left(\frac{\partial w_0}{\partial r}\right)^3 + M^2(w_0 + 1) + \frac{\partial P_1}{\partial z}$$

Second Order:

$$L(w_2) = -\alpha\left(\frac{\partial w_1}{\partial r}\right) - \beta\left(\frac{\partial w_0}{\partial r}\right)\left(\frac{\partial w_1}{\partial r}\right) + M^2 w_1 + \frac{\partial P_1}{\partial z}$$

Zeroth Order Solution:

$$L(w_0) = L(w_{10})$$

$$w_0 = -1 - 2\pi\epsilon\delta\gamma\cos(2\pi z) + \left(\frac{r^2 - h^2}{4}\right)P_0$$

First Order Solution:

$$w_1 = -\frac{r^2}{4}P_0 - \alpha\frac{r^3}{18}P_0 - \beta\frac{r^5}{200}{P_0}^3 + M^2\left(\frac{-\pi r^2}{2}\epsilon\delta\gamma\cos(2\pi z) + \left(\frac{r^4}{16} - \frac{r^2 h^2}{16}\right)P_0\right) - \frac{r^2}{4}$$

Second Order Solution:

$$w_2=\alpha\frac{r^3}{8}P_0+\alpha^2\frac{r^4}{24}P_0+\alpha\beta\frac{r^6}{160}{P_0}^3-M^2\alpha\left(\frac{-\pi r^3}{4}\epsilon\delta\gamma\cos(2\pi z)+\left(\frac{r^4}{16}-\frac{r^3h^2}{32}\right)P_0\right)-\alpha\frac{r^3}{8}P_1+\beta\frac{r^4}{32}{P_0}^2+\alpha\beta\frac{r^5}{300}{P_0}^2+\beta^2\frac{r^7}{3920}{P_0}^4-M^2\beta\left(\frac{-\pi r^4}{32}\epsilon\delta\gamma\cos(2\pi z)P_0+\left(\frac{r^6}{144}-\frac{r^4h^2}{128}\right){P_0}^2\right)-\beta\frac{r^4}{64}P_0P_1+M^2\left(-\frac{r^4}{64}P_0-\alpha\frac{r^5}{450}P_0-\beta\frac{r^7}{9800}{P_0}^3+M^2\left(\frac{-\pi r^4}{32}\epsilon\delta\gamma\cos(2\pi z)+\left(\frac{r^6}{576}-\frac{r^4h^2}{256}\right)P_0\right)\right)+\frac{r^5}{80}P_1+\frac{r^2}{4}P_2$$

$$w = w_0 + w_1 + w_2$$

For embedded parameter $q\to1$, an analytical solution of velocity and the exact solution for an equation involving concentration and temperature will be written.

$$w=-1-2\pi\epsilon\delta\gamma\cos(2\pi z)+\alpha^2\left(\frac{r^4-h^4}{24}\right)P_0-\alpha\beta\left(\frac{r^6-h^6}{160}\right){P_0}^3+M^2\alpha\left(-\pi\left(\frac{r^3-h^3}{4}\right)\epsilon\delta\gamma\cos(2\pi z)+\left(\frac{r^4-h^4}{16}-\frac{(r^3-h^3)h^2}{32}\right)P_0\right)-\alpha\left(\frac{r^3-h^3}{8}\right)P_1+\beta\left(\frac{r^4-h^4}{32}\right){P_0}^2-\alpha\beta\left(\frac{r^5-h^5}{300}\right){P_0}^2+\beta\left(\frac{r^4-h^4}{3920}\right){P_0}^4-M^2\beta\left(-\pi\left(\frac{r^4-h^4}{3}\right)\epsilon\delta\gamma\cos(2\pi z)P_0+\left(\frac{r^6-h^6}{144}-\frac{(r^4-h^4)h^2}{128}\right){P_0}^2\right)-\beta\left(\frac{r^4-h^4}{64}\right)P_0P_1+M^2\left(\left(-\left(\frac{r^4-h^4}{644}\right)P_0-\alpha\left(\frac{r^5-h^5}{450}\right)P_0-\beta\left(\frac{r^7-h^7}{9800}\right){P_0}^3+M^2\left(-\pi\left(\frac{r^4-h^4}{32}\right)\epsilon\delta\gamma\cos(2\pi z)+\left(\frac{r^6-h^6}{576}-\frac{(r^4-h^4)h^2}{256}\right)P_0\right)\right)+\left(\frac{r^5-h^5}{80}\right)P_1\right)+\frac{r^5-h^5}{80}P_2 \tag{21}$$

3.3. The solution of temperature and concentration are defined as

$$\theta=A_1\left(A_2\left(r^{17}-h^{17}\right)-A_3\left(r^{18}-h^{18}\right)-A_4\left(r^{16}-h^{16}\right)-A_5\left(r^5-h^5\right)-A_6\left(r^4-h^4\right)-A_7\left(r^{14}-h^{14}\right)-A_8\left(r^{15}-h^{15}\right)-A_9\left(r^{13}-h^{13}\right)-A_{10}\left(r^{11}-h^{11}\right)-A_{11}\left(r^{12}-h^{12}\right)-A_{12}\left(r^{10}-h^{10}\right)-A_{13}\left(r^8-h^8\right)-A_{14}\left(r^7-h^7\right)-A_{15}\left(r^9-h^9\right)-A_{16}\left(r^6-h^6\right) \tag{22}$$

And

$$\sigma=B_1\left(B_2\left(r^{19}-h^{19}\right)+B_3\left(r^{20}-h^{20}\right)+B_4\left(r^{18}-h^{18}\right)+B_5\left(r^7-h^7\right)+B_6\left(r^6-h^6\right)+B_7\left(r^{16}-h^{16}\right)+B_8\left(r^{17}-h^{17}\right)+B_9\left(r^{15}-h^{15}\right)+B_{10}\left(r^{13}-h^{13}\right)+B_{11}\left(r^{14}-h^{14}\right)+B_{12}\left(r^{12}-h^{12}\right)+B_{13}\left(r^{10}-h^{10}\right)+B_{14}\left(r^9-h^9\right)+B_{15}\left(r^{11}-h^{11}\right)+B_{16}\left(r^8-h^8\right) \tag{23}$$

Where the other constraints can be written as:

$$A_1=\frac{1}{21171870720000}B, A_2=\frac{19459440}{17}{P_0}^9\beta^4, A_3=\frac{51051}{2}{P_0}^{12}\beta^5, A_4=\frac{6891885}{16}{P_0}^6\beta^3\left(45+2{P_0}^4\alpha\beta\right), A_5=35286451200P_0\alpha^2\left(h^2+4P_1+8M^2\pi\epsilon\delta\gamma\cos2\pi z\right),$$

$$A_6=20675655000\alpha\left(h^2+4P_1+8M^2\pi\epsilon\delta\gamma\cos2\pi z\right)^2, A_7=\frac{19691100}{7}\beta\left(150+120{P_0}^4\alpha\beta-9{P_0}^6\left(h^2+4P_1\right)\beta^2+4{P_0}^8\alpha^2\beta^2-72M^2{P_0}^6\pi\beta^2\epsilon\delta\gamma\cos2\pi z\right),$$

$$A_8=\frac{3675672}{5}{P_0}^3\beta^2\left(-200-40{P_0}^4\alpha\beta+{P_0}^6\left(h^2+4P_1\right)\beta^2+8M^2{P_0}^6\pi\beta^2\epsilon\delta\gamma\cos2\pi z\right),$$

$$A_9=\frac{84823200}{13}P_0\beta\left(45{P_0}^2\left(h^2+4P_1\right)\beta-40{P_0}^4\alpha^2\beta+\alpha\left(-200+3h^2{P_0}^6+12{P_0}^6P_1\beta^2\right)+24M^2{P_0}^2\pi\beta\left(15+{P_0}^4\alpha\beta\right)\epsilon\delta\gamma\cos2\pi z\right),$$

$$A_{10}=\frac{27846000}{11}\beta P_0\left(-81h^4{P_0}^2\beta+72h^2\left(15\alpha-9{P_0}^2P_1\beta+{P_0}^4\alpha^2\beta\right)+16\left(-20{P_0}^2\alpha^3-81{P_0}^2{P_1}^2\beta+81P_1\alpha\left(15+{P_0}^4\alpha\beta\right)\right)+144M^2\pi\left(60\alpha-9{P_0}^2\left(h^2+4P_1\right)\beta+4{P_0}^4\alpha^2\beta\right)\epsilon\delta\gamma\cos2\pi z-5184M^4{P_0}^2\pi^2\beta\epsilon\delta\gamma\cos\left(2\pi z\right)^2\right),$$

$$A_{11}=\frac{425425}{4}\beta\left(81h^4{P_0}^6\beta^2+216h^2\left(-50-20{P_0}^4\alpha\beta+3{P_0}^6P_1\beta^2\right)+16\left(81{P_0}^6{P_1}^2\beta^2-540P_1\left(5+2{P_0}^4\alpha\beta\right)+20{P_0}^2\alpha^2\left(45+2{P_0}^4\alpha\beta\right)\right)+432M^2\pi\left(-200-80{P_0}^4\alpha\beta+3{P_0}^6\left(h^2+4P_1\right)\beta^2\right)\epsilon\delta\gamma\cos2\pi z+5184M^4{P_0}^6\pi^2\beta^2\epsilon\delta\gamma\cos\left(2\pi z\right)^2\right),$$

$$A_{12}=204204\beta\left(405h^4\left(15+2{P_0}^4\alpha\beta\right)+8\left(-5400{P_0}^2P_1\alpha^2+100{P_0}^4\alpha^4+81{P_0}^6\alpha\beta+810{P_1}^2\left(15+2{P_0}^4\alpha\beta\right)\right)+1080h^2\left(-10{P_0}^2\alpha^2+P_1\left(45+6{P_0}^4\alpha\beta\right)\right)+2160M^2\pi\left(h^2\left(45+6{P_0}^4\alpha\beta\right)+4\left(45P_1-10{P_0}^2\alpha^2+6{P_0}^4P_1\alpha\beta\right)\right)\epsilon\delta\gamma\cos2\pi z+25920M^4\pi^2\left(15+2{P_0}^4\alpha\beta\right)\epsilon\delta\gamma\cos\left(2\pi z\right)^2\right),$$

$$A_{13}=\frac{172297125}{4}\left(480\alpha-15\left(h^2+4P_1\right)^3\beta+4{P_0}^2\left(5h^4+16{P_0}^2+40h^2P_1+80{P_1}^2\right)\alpha^2\beta-40M^2\pi\left(9h^4+16P_1\left(9P_1-2{P_0}^2\alpha^2\right)+8h^2\left(9P_1-{P_0}^2\alpha^2\right)\right)\beta\epsilon\delta\gamma\cos2\pi z-320M^4\pi^2\left(9h^2+36P_1-4{P_0}^2\alpha^2\right)\beta\epsilon\delta\gamma\cos\left(2\pi z\right)^2-7680M^6\pi^3\beta\epsilon\delta\gamma\cos\left(2\pi z\right)^3\right),$$

$$A_{14}=\frac{787644000}{7}P_0\alpha\left(-320\alpha+\left(h^2+4P_1\right)\left(5h^4+24{P_0}^2+40h^2P_1+80{P_1}^2\right)\beta+24M^2\left(5h^4+8{P_0}^2+40h^2P_1+80{P_1}^2\right)\pi\beta\epsilon\delta\gamma\cos2\pi z+960M^2\left(h^2+4P_1\right)\pi^2\beta\epsilon\delta\gamma\cos\left(2\pi z\right)^2+2560M^6\pi^3\beta\epsilon\delta\gamma\cos\left(2\pi z\right)^3\right),$$

$$A_{15}=\frac{17017000}{9}P_0\beta\left(27h^6{P_0}^2\beta-108h^4\left(10\alpha-3{P_0}^2P_1\beta\right)+16h^2\left(-540P_1\alpha+20{P_0}^2\alpha^3+81{P_0}^2{P_1}^2\beta\right)+64\left(-270{P_1}^2\alpha+{P_0}^2\left(-27\alpha+20P_1\alpha^3+27{P_1}^3\beta\right)\right)+8M^4\pi\left(81h^4{P_0}^2\beta-216h^2\left(10\alpha-3{P_0}^2P_1\beta\right)+16\left(-540P_1\alpha+20{P_0}^2\alpha^3+81{P_0}^2{P_1}^2\beta\right)\right)\epsilon\delta\gamma\cos2\pi z-1728M^4\pi^2\left(40\alpha-3{P_0}^2\left(h^2+4P_1\right)\beta\right)\epsilon\delta\gamma\cos\left(2\pi z\right)^2+13824M^6{P_0}^2\pi^3\beta\epsilon\delta\gamma\cos\left(2\pi z\right)^3\right),$$

$$A_{16}=\frac{31906875}{2}\left(9h^8\beta+144h^6P_1\beta+864h^4{P_1}^2\beta-2304h^2\left(\alpha-{P_1}^3\beta\right)+256\left(-36P_1\alpha+4{P_0}^2\alpha^3+9{P_1}^4\beta\right)-288M^2\pi\left(64\alpha-\left(h^2+4P_1\right)^3\beta\right)\epsilon\delta\gamma\cos2\pi z+3456M^4\left(h^2+4P_1\right)^2\pi^2\beta\epsilon\delta\gamma\cos\left(2\pi z\right)^2+18432M^6\left(h^2+4P_1\right)\pi^3\beta\epsilon\delta\gamma\cos\left(2\pi z\right)^3+36864M^8\pi^4\beta\epsilon\delta\gamma\cos\left(2\pi z\right)^4\right),$$

Furthermore:

$$B_1 = \frac{1}{21171870720000}BST, B_2 = -\frac{19459440}{19}{P_0}^9\beta^4, B_3 = \frac{459459}{20}{P_0}^{12}\beta^5, B_4 = \frac{765765}{2}{P_0}^6\beta^3\left(45+2{P_0}^4\alpha\beta\right), B_5 = 25204608000P_0\alpha^2\left(h^2+4P_1+8M^2\pi\epsilon\delta\gamma\cos 2\pi z\right),$$

$$B_6 = 13783770000\alpha\left(h^2+4P_1+8M^2\pi\epsilon\delta\gamma\cos 2\pi z\right)^2, B_7 = \frac{4922775}{2}\beta\left(150+120{P_0}^4\alpha\beta-9{P_0}^6\left(h^2+4P_1\right)\beta^2+4{P_0}^8\alpha^2\beta^2-72M^2{P_0}^6\pi\beta^2\epsilon\delta\gamma\cos 2\pi z\right),$$

$$B_8 = 648648{P_0}^3\beta^2\left(-200-40{P_0}^4\alpha\beta+{P_0}^6\left(h^2+4P_1\right)\beta^2+8M^2{P_0}^6\pi\beta^2\epsilon\delta\gamma\cos 2\pi z\right),$$

$$B_9 = 5654880P_0\beta\left(45{P_0}^2\left(h^2+4P_1\right)\beta-40{P_0}^4\alpha^2\beta+\alpha\left(-200+3h^2{P_0}^6+12{P_0}^6P_1\beta^2\right)+24M^2{P_0}^2\pi\beta\left(15+{P_0}^4\alpha\beta\right)\epsilon\delta\gamma\cos 2\pi z\right),$$

$$B_{10} = 2142000\beta P_0\left(-81h^4{P_0}^2\beta+72h^2\left(15\alpha-9{P_0}^2P_1\beta+{P_0}^4\alpha^2\beta\right)+16\left(-20{P_0}^2\alpha^3-81{P_0}^2{P_1}^2\beta+81P_1\alpha\left(15+{P_0}^4\alpha\beta\right)\right)+144M^2\pi\left(60\alpha-9{P_0}^2\left(h^2+4P_1\right)\beta+4{P_0}^4\alpha^2\beta\right)\epsilon\delta\gamma\cos 2\pi z-5184M^4{P_0}^2\pi^2\beta\epsilon\delta\gamma\cos\left(2\pi z\right)^2\right),$$

$$B_{11} = \frac{182325}{2}\beta\left(81h^4{P_0}^6\beta^2+216h^2\left(-50-20{P_0}^4\alpha\beta+3{P_0}^6P_1\beta^2\right)+16\left(81{P_0}^6{P_1}^2\beta^2-540P_1\left(5+2{P_0}^4\alpha\beta\right)+20{P_0}^2\alpha^2\left(45+2{P_0}^4\alpha\beta\right)\right)+432M^2\pi\left(-200-80{P_0}^4\alpha\beta+3{P_0}^6\left(h^2+4P_1\right)\beta^2\right)\epsilon\delta\gamma\cos 2\pi z+5184M^4{P_0}^6\pi^2\beta^2\epsilon\delta\gamma\cos\left(2\pi z\right)^2\right),$$

$$B_{12} = 170170\beta\left(405h^4\left(15+2{P_0}^4\alpha\beta\right)+8\left(-5400{P_0}^2P_1\alpha^2+100{P_0}^4\alpha^4+81{P_0}^6\alpha\beta+810{P_1}^2\left(15+2{P_0}^4\alpha\beta\right)\right)+1080h^2\left(-10{P_0}^2\alpha^2+P_1\left(45+6{P_0}^4\alpha\beta\right)\right)+2160M^2\pi\left(h^2\left(45+6{P_0}^4\alpha\beta\right)+4\left(45P_1-10{P_0}^2\alpha^2+6{P_0}^4P_1\alpha\beta\right)\right)\epsilon\delta\gamma\cos 2\pi z+25920M^4\pi^2\left(15+2{P_0}^4\alpha\beta\right)\epsilon\delta\gamma\cos\left(2\pi z\right)^2\right),$$

$$B_{13} = 34459425\left(480\alpha-15\left(h^2+4P_1\right)^3\beta+4{P_0}^2\left(5h^4+16{P_0}^2+40h^2P_1+80{P_1}^2\right)\alpha^2\beta-40M^2\pi\left(9h^4+16P_1\left(9P_1-2{P_0}^2\alpha^2\right)+8h^2\left(9P_1-{P_0}^2\alpha^2\right)\right)\beta\epsilon\delta\gamma\cos 2\pi z-320M^4\pi^2\left(9h^2+36P_1-4{P_0}^2\alpha^2\right)\beta\epsilon\delta\gamma\cos\left(2\pi z\right)^2-7680M^6\pi^3\beta\epsilon\delta\gamma\cos\left(2\pi z\right)^3\right),$$

$$B_{14} = 87516000P_0\alpha\left(-320\alpha+\left(h^2+4P_1\right)\left(5h^4+24{P_0}^2+40h^2P_1+80{P_1}^2\right)\beta+24M^2\left(5h^4+8{P_0}^2+40h^2P_1+80{P_1}^2\right)\pi\beta\epsilon\delta\gamma\cos 2\pi z+960M^2\left(h^2+4P_1\right)\pi^2\beta\epsilon\delta\gamma\cos\left(2\pi z\right)^2+2560M^6\pi^3\beta\epsilon\delta\gamma\cos\left(2\pi z\right)^3\right),$$

$$B_{15} = 1547000P_0\beta\left(27h^6{P_0}^2\beta-108h^4\left(10\alpha-3{P_0}^2P_1\beta\right)+16h^2\left(-540P_1\alpha+20{P_0}^2\alpha^3+81{P_0}^2{P_1}^2\beta\right)+64\left(-270{P_1}^2\alpha+{P_0}^2\left(-27\alpha+20P_1\alpha^3+27{P_1}^3\beta\right)\right)+8M^4\pi\left(81h^4{P_0}^2\beta-216h^2\left(10\alpha-3{P_0}^2P_1\beta\right)+16\left(-540P_1\alpha+20{P_0}^2\alpha^3+81{P_0}^2{P_1}^2\beta\right)\epsilon\delta\gamma\cos 2\pi z-1728M^4\pi^2\left(40\alpha-3{P_0}^2\left(h^2+4P_1\right)\beta\right)\epsilon\delta\gamma\cos\left(2\pi z\right)^2+13824M^6{P_0}^2\pi^3\beta\epsilon\delta\gamma\cos\left(2\pi z\right)^3\right),$$

$$B_{16} = \frac{95720625}{8}\left(9h^8\beta+144h^6P_1\beta+864h^4{P_1}^2\beta-2304h^2\left(\alpha-{P_1}^3\beta\right)+256\left(-36P_1\alpha+4{P_0}^2\alpha^3+9{P_1}^4\beta\right)-288M^2\pi\left(64\alpha-\left(h^2+4P_1\right)^3\beta\right)\epsilon\delta\gamma\cos 2\pi z+3456M^4\left(h^2+4P_1\right)^2\pi^2\beta\epsilon\delta\gamma\cos\left(2\pi z\right)^2+18432M^6\left(h^2+4P_1\right)\pi^3\beta\epsilon\delta\gamma\cos\left(2\pi z\right)^3+36864M^8\pi^4\beta\epsilon\delta\gamma\cos\left(2\pi z\right)^4\right)$$

Stream Function:

$$w = \frac{1}{r}\frac{\partial\psi}{\partial r},\ u = -\frac{1}{r}\frac{\partial\psi}{\partial Z}$$

Stream Function Solution:

$$\psi = -\frac{r^2}{2}-\pi r^2\epsilon\delta\gamma\cos(2\pi z)+\alpha\left(\frac{2r^5-5r^2h^3}{180}\right)P_0-\beta\left(\frac{2r^7-7r^2h^5}{64}\right){P_0}^3+M^2\left(-\pi\left(\frac{r^4-2r^2h^2}{8}\right)\epsilon\delta\gamma\cos(2\pi z)+\left(\frac{r^4-2r^2h^2}{64}-\frac{r^4h^2-r^2h^4}{64}\right)P_0\right)-\left(\frac{r^4-2r^2h^2}{64}\right)P_1$$

We have considered $S_T = T,\ S_h = S$.

The coefficient of heat transfer at the wall is given by $Z = h_z\theta_r$

4. Results and discussions

The non-dimensional variables used in this study are M, B, S, T, α, β, γ, and δ. Unless otherwise specified in the figures, these parameter values remain fixed throughout the analysis. Figs. 2a–2d show a decrease in the temperature profile and a corresponding increase in the concentration profile as the Soret number increases. The Soret number, defined as the ratio of the diffusion coefficient to the thermodiffusion coefficient, increases with the temperature difference.

Fig. 3a shows that the parameter σ increases as the fluid parameter T rises across the entire region. In Fig. 3b, σ increases with increasing values of B, while Fig. 3c shows that σ also rises with increasing T.

From Figs. 4a and 4b, it is observed that as α and β increase, the temperature rises while both velocity and concentration decrease. The momentum of the boundary layer is reduced due to the increase in the magnetic attraction parameter, particularly when the fluid's electrical conductivity-to-density ratio is low. Physically, this is attributed to the drag force that opposes the flow, which becomes more pronounced at higher values of α and β, potentially leading to a thinner momentum boundary layer.

Fig. 4c clearly demonstrates that an increase in the velocity slip parameter leads to a decrease in velocity and an increase in both temperature and concentration profiles. The flow velocity is crucial for dissipating heat from the surface. Physically, heat generated by viscous dissipation affects the thermal boundary layer thickness. In high-speed flows, such as in aerodynamics, viscous heating significantly influences thermal distribution within the boundary layer. In microfluidic systems, viscous dissipation becomes dominant due to small characteristic length scales. The slip parameter near the surface reduces the flow

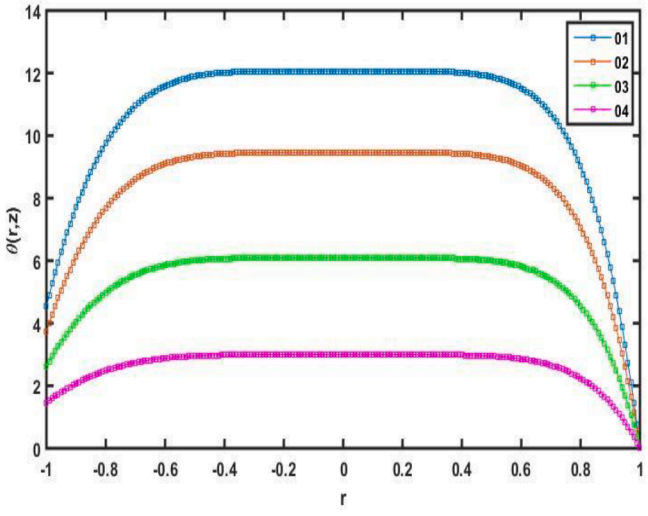

Fig. 2a. Influence of M on temperature with $\delta = 1.8, \alpha = 0.3, \gamma = 0.5, \beta = 1.8, B = 0.7$.

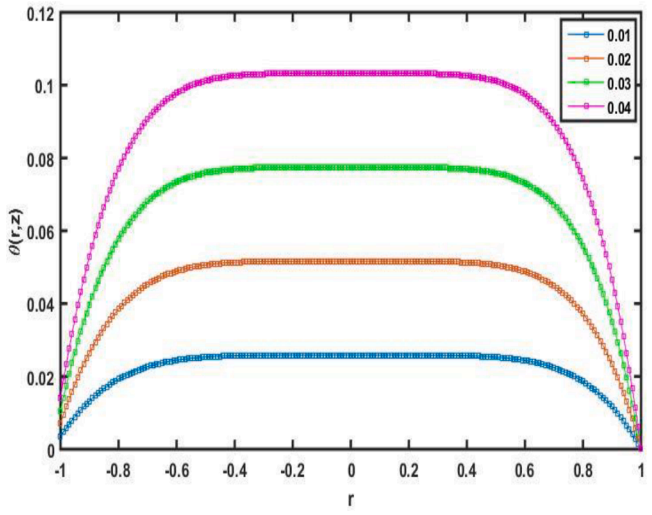

Fig. 2b. Influence of B on temperature with $M = 0.3, \delta = 0.8, \alpha = 0.2, \gamma = 0.5, \beta = 0.3$.

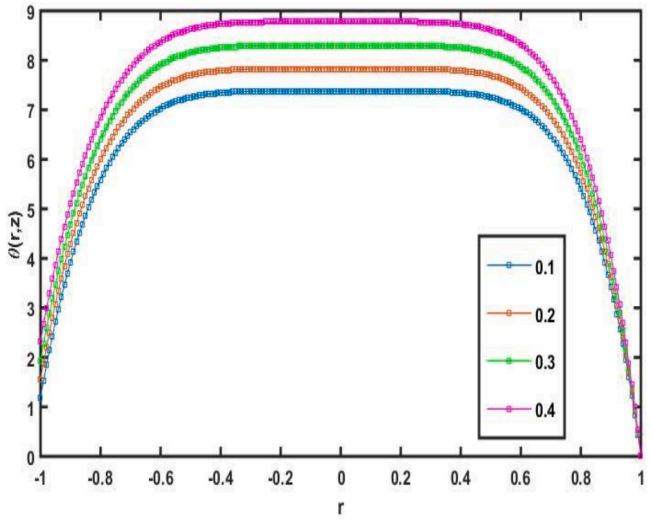

Fig. 2c. Influence of α on temperature with $\delta = 1.5, \gamma = 1.3, \beta = 0.7, M = 0.4, B = 1.1$.

velocity, which in turn increases the temperature. Generally, increasing slip enhances wall friction and introduces additional heat into the flow.

Cilia play a vital role in various biological and physiological processes by facilitating fluid movement, particle transport, and maintaining homeostasis in living organisms. Their rhythmic contraction and relaxation cycles generate propulsion, which is essential for numerous functions. For instance, cilia lining the respiratory tract help clear mucus and trapped particles, thereby preventing infections. In the fallopian tubes, cilia assist in transporting ova toward the uterus. In the brain ventricles, cilia contribute to the circulation of cerebrospinal fluid, helping to maintain intracranial pressure.

Figs. 5a–5d illustrate the influence of the pressure gradient. Fig. 5a shows that a pressure gradient develops in the regions $z \in [-0.5,\ 0.5]$ and $z \in [0.5,\ 1.5]$, where the flow slows down or becomes stationary. The appearance of multi-sinusoidal waves indicates that as the value of γ increases, the pressure gradient becomes more pronounced in specific regions and stabilizes at certain values of γ.

Fig. 5b demonstrates that an increase in α results in a decrease in the pressure gradient. Fig. 5c shows that the pressure gradient increases with the rise in δ. Fig. 5d reveals that the pressure gradient also increases

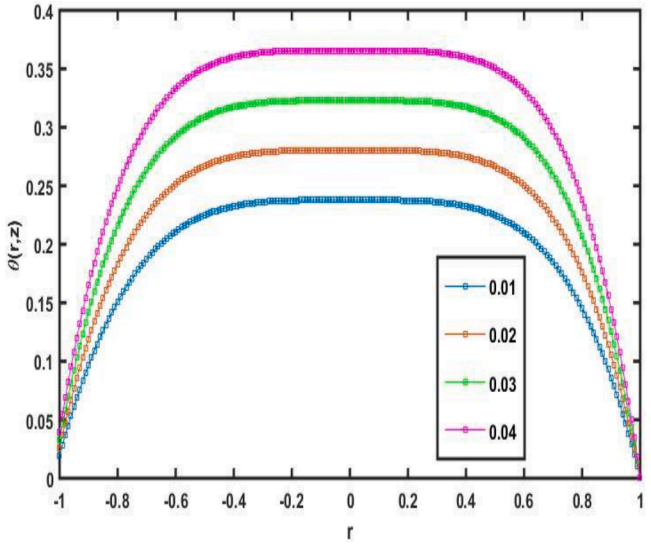

Fig. 2d. Influence of β on temperature with $\delta = 1.8, \gamma = 0.5, M = 1.8, \alpha = 0.3, B = 0.7$.

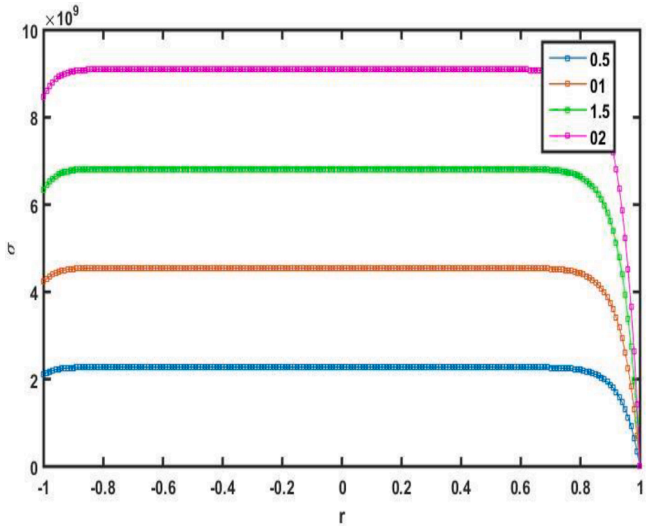

Fig. 3a. Sigma graph for B with $S = 0.1, T = 0.3, \delta = 0.7, \gamma = 0.3, \beta = -1.2, M = 0.5, \alpha = 0$.

with β, but only in specific regions.

Figs. 6a and 6b show that with an increasing β, the pressure rise decreases with respect to M. Figs. 7a–7b and 8a–8b depict the influence of increasing pressure for various linear values of δ, β, and M on the flow rate. These figures indicate that as the parametric values α, β, αF, and δ increase, the pressure development rises. The corresponding flow rate increases in the region $[-1.0,\ -0.5]$, then rises again in the region $[1.0,\ 2.0]$, while the pressure rise decreases in specific regions associated with β and F. Figures 9a–9d depict streamlines that form a characteristic bolus shape, consistent with the geometry under consideration.

5. Concluding Remarks

In this study, we analytically explored the effects of viscous dissipation on cilia-induced Prandtl fluid flow within a horizontal tube. By applying the Homotopy Perturbation Method (HPM), approximate solutions for temperature and velocity profiles were derived from the governing nonlinear equations. A detailed investigation was conducted to examine the influence of critical parameters, including the Prandtl

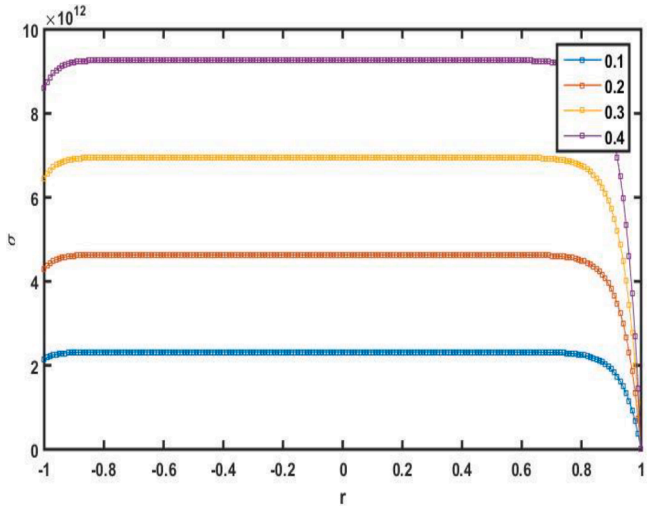

Fig. 3b. Sigma graph for S with $T = 1.1, \alpha = 0.7 \delta = 1.7, \gamma = 0.3, \beta = -3.7, M = 0.1, B = 0.5$.

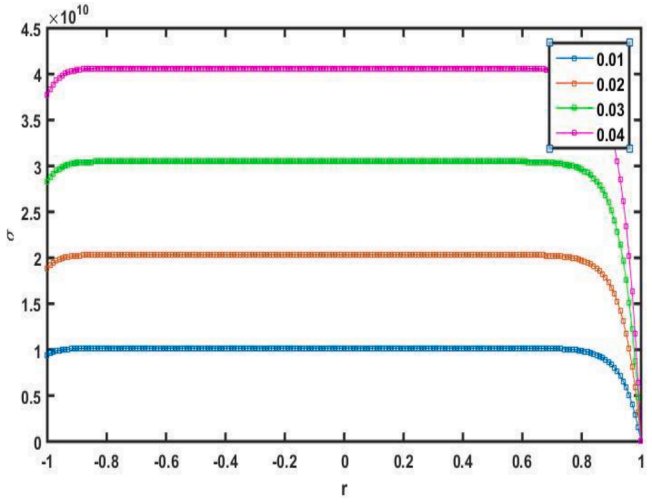

Fig. 3c. Sigma graph for T with $S = 0.1, \alpha = 1.1, \delta = 0.5, \gamma = 0.3, \beta = -3.2, M = 0.7, B = 0.5$.

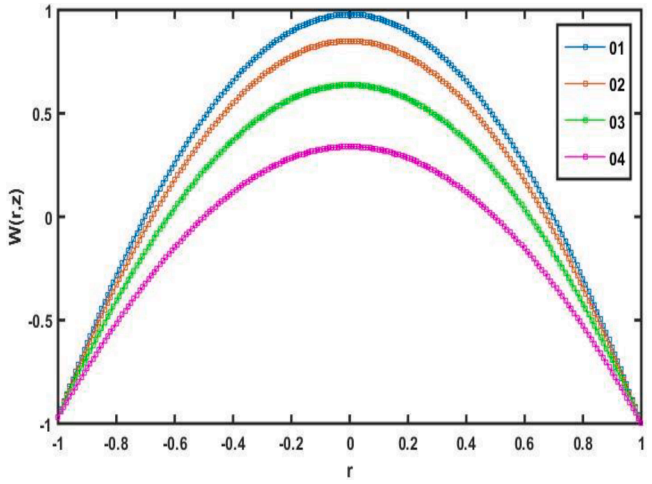

Fig. 4a. Effect of M on velocity with $\beta = 0.1,\ \alpha = 0.1\ \delta = 1.8, \gamma = 0.8$.

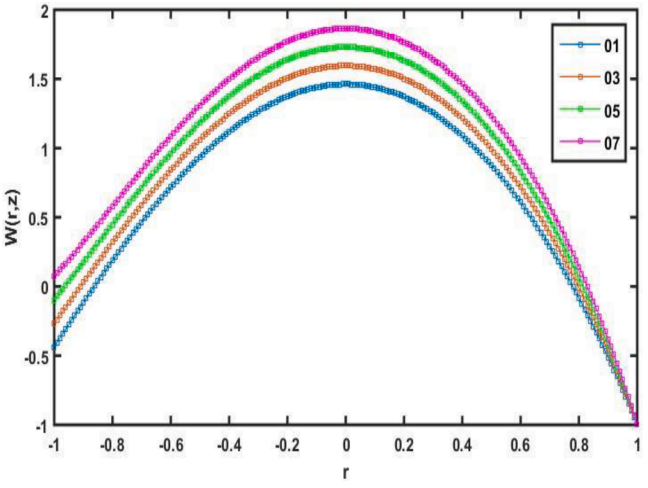

Fig. 4b. Effect of β on velocity with $\alpha = 2.1, \delta = 1.8, \gamma = 2.1, M = 0.8$.

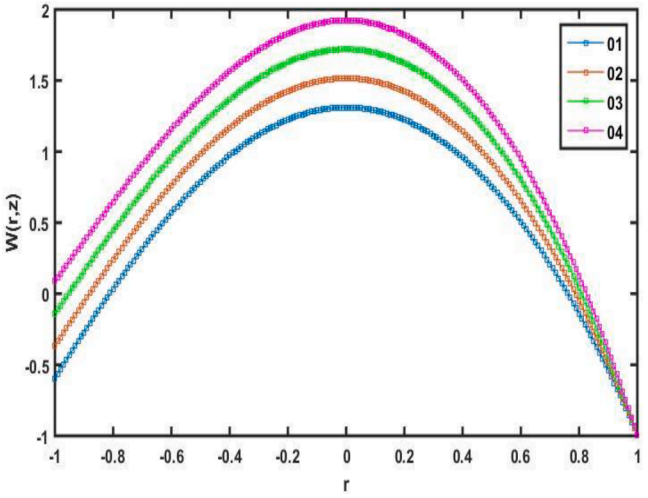

Fig. 4c. Effect of α on velocity $\beta = 2.1$ with $\delta = 1.8, \gamma = 2.1, M = 0.8$.

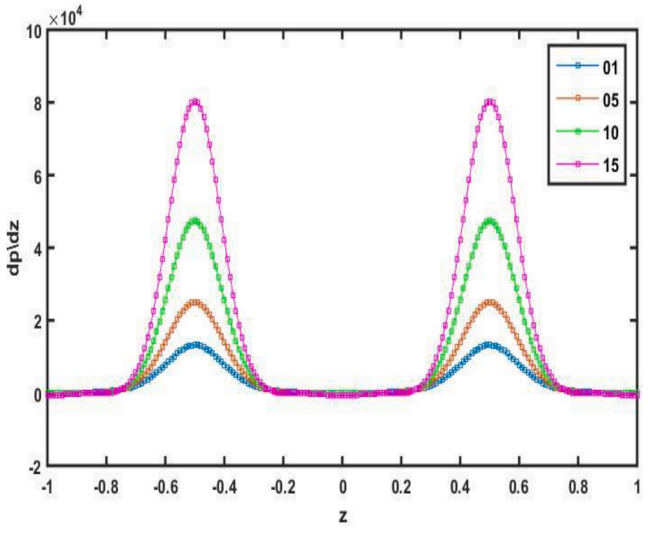

Fig. 5a. Effect of γ on $\frac{dp}{dz}$ with $\delta = 0.4, \alpha = 0.8, \beta = 1.3, M = 0.1$.

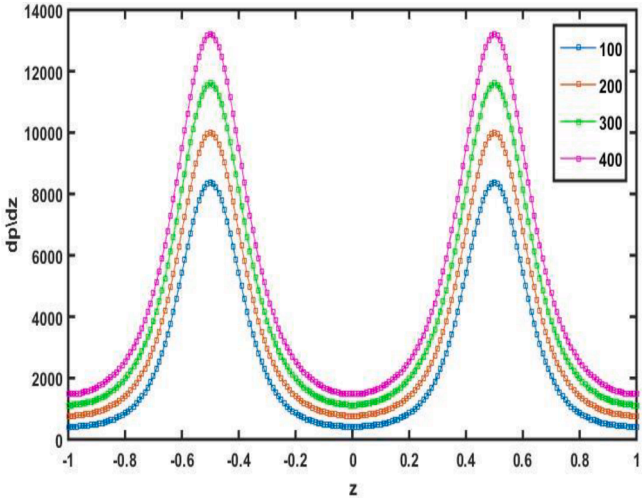

Fig. 5b. Effect of α on $\frac{dp}{dz}$ with $M = 1.3, \gamma = 0.4, \beta = 0.8, \delta = 0.01$.

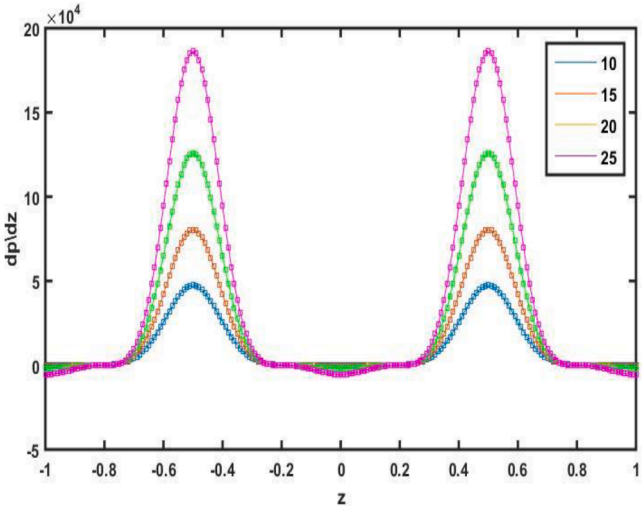

Fig. 5c. Effect of δ on $\frac{dp}{dz}$ with $M = 1.1, \gamma = 0.4, \beta = 1.3, \alpha = 1.8$.

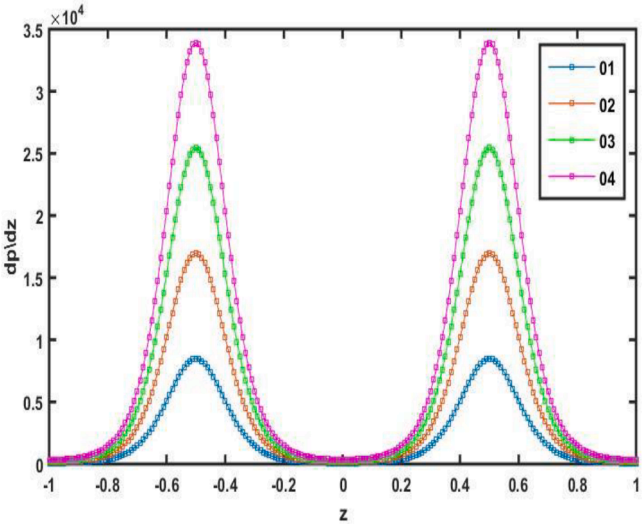

Fig. 5d. Effect of β on $\frac{dp}{dz}$ with $\delta = 0.01, \alpha = 0.8, \gamma = 0.4, M = 1.3$.

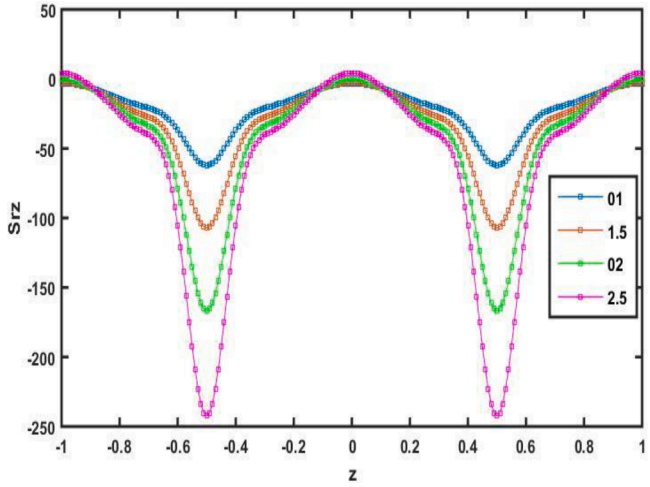

Fig. 6a. Effect of β on S_{rz} with $M = 2.6, \gamma = 0.1, \ \delta = 0.8, \alpha = 1.8$.

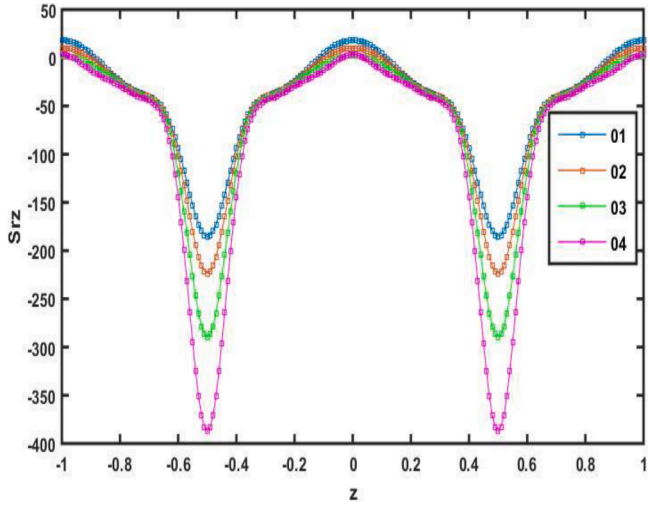

Fig. 6b. Effect of M on S_{rz} with $\delta = 0.8, \alpha = 1.8, \gamma = 0.1, \beta = 2.7$.

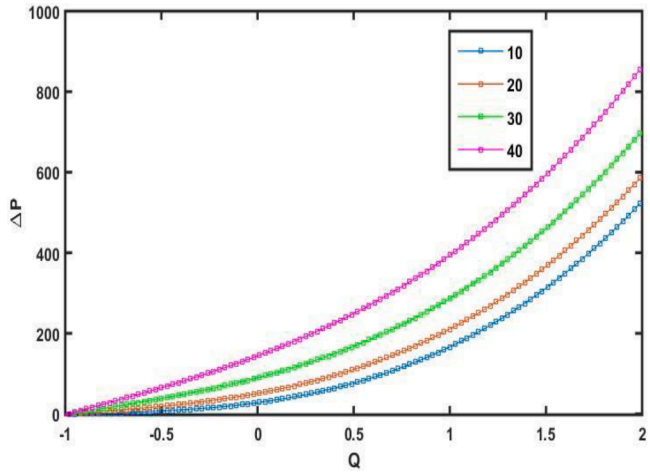

Fig. 7a. Pressure rise for δ with $M = 0.1, \gamma = 0.4, \beta = 0.8, \alpha = 0.01$.

number, viscosity ratio, magnetic field, and ciliary motion characteristics, on flow dynamics and heat transfer. The model successfully incorporates viscous effects, often neglected in prior research, and

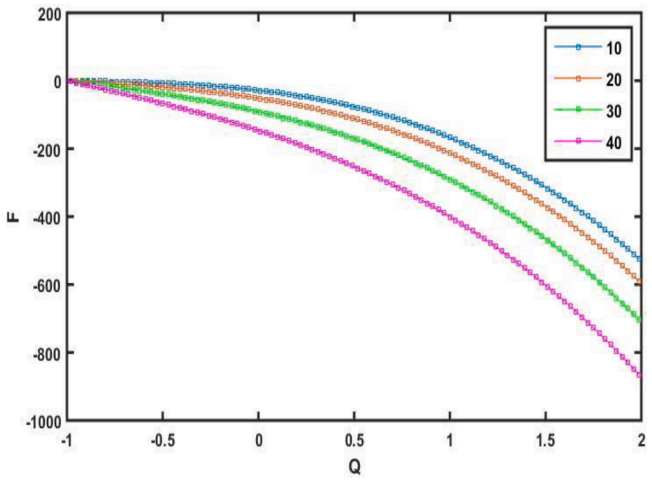

Fig. 7b. Pressure rise for δF with $M = 0.1, \gamma = 0.4, \beta = 0.8, \alpha = 0.01$.

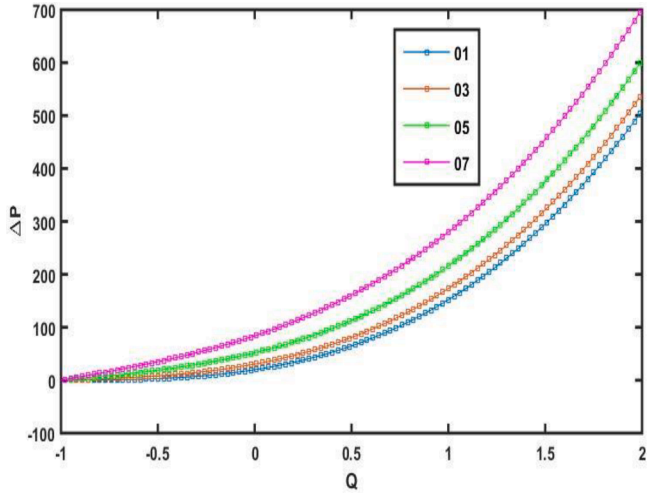

Fig. 8a. Pressure rise for M with $\alpha = 0.1, \gamma = 1.7, \beta = -0.4, \delta = 1.3$.

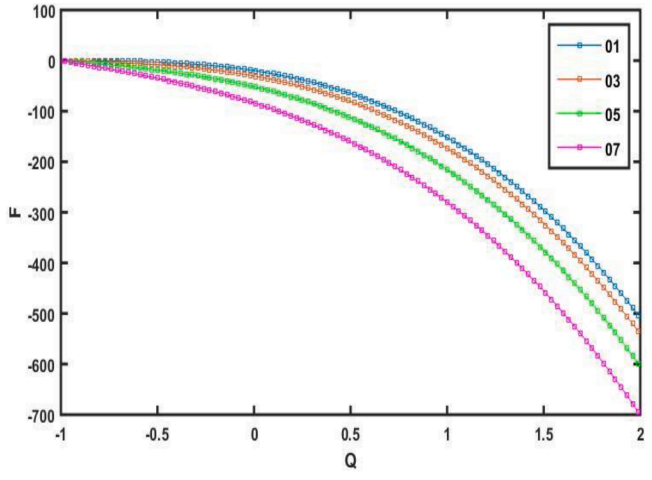

Fig. 8b. Frictional forces for MF with $\alpha = 0.1, \gamma = 1.7, \beta = -0.4, \delta = 1.3$.

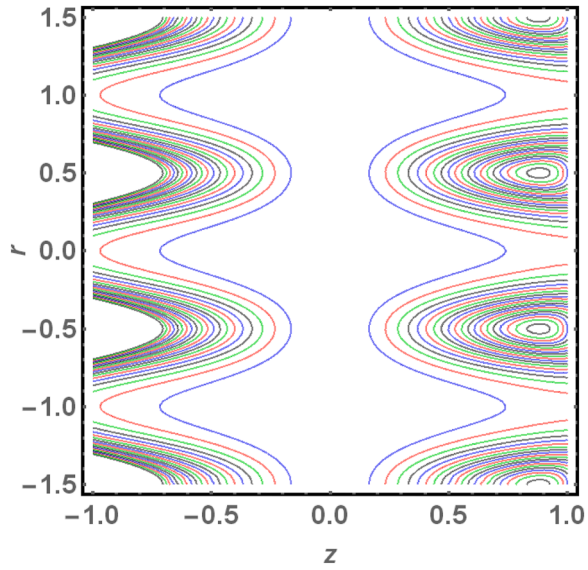

Fig. 9a. Streamline graph for α with $\beta = 0.7, M = 0.3, \delta = 1.4, \gamma = 0.1$.

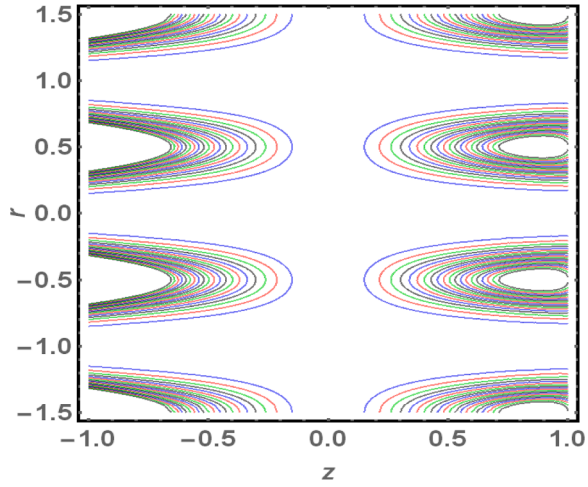

Fig. 9b. Streamline graph for β with $\alpha = 0.3, M = 0.1, \delta = 0.7, \gamma = 1.4$.

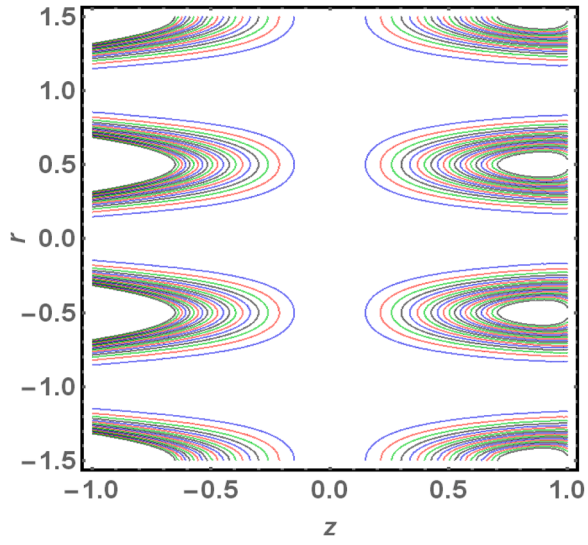

Fig. 9c. Streamline graph for δ with $\beta = 0.7, M = 0.1, \alpha = 0.3, \gamma = 1.4$.

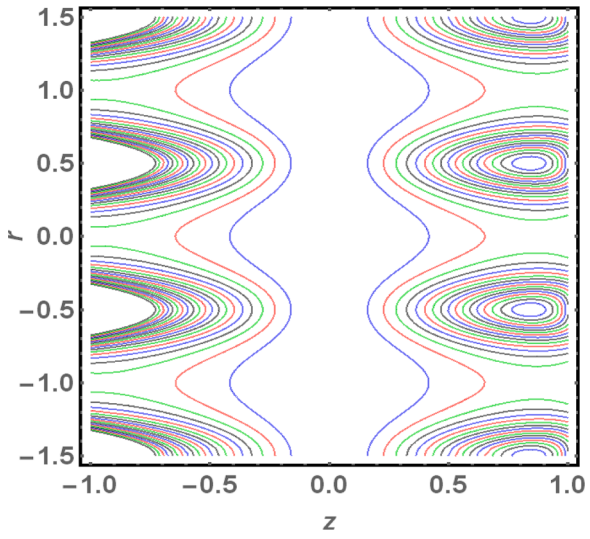

Fig. 9d. Streamline graph for M with $\alpha = 0.3, \beta = 0.7, \delta = 1.4, \gamma = 0.5$.

highlights the substantial modifications in the thermal and velocity fields due to energy dissipation. This work not only improves the physical realism of physiological and industrial transport simulations but also demonstrates the precision and efficiency of HPM in solving complex fluid dynamics problems. The major findings of the study are summarized below:

- As the magnetic parameter M increases, the axial velocity field is suppressed due to enhanced Lorentz forces, leading to an increase in fluid temperature.
- Increasing fluid parameters such as α, β, and B results in a reduction in velocity, while both temperature and thermal boundary layer thickness exhibit a rising trend; however, higher values of M lead to a decrease in these thermal properties.
- Cilia-induced motion is modeled as regular and periodic, and the small parameter approximation effectively captures the role of viscous dissipation in the flow behavior.
- The flow satisfies the physical boundary conditions of a zero axial pressure gradient at infinity and no-slip conditions at the tube walls.
- Pressure rise exhibits a direct correlation with increasing δ and M, while other flow parameters generally show an inverse relationship with pressure development.
- Near the tube walls, an increase in ε (from 0.01 to 0.1) leads to a noticeable rise (approximately 15–25 %) in peak fluid temperature.
- Higher Prandtl numbers (Pr) values (from 5 to 20) produce steeper thermal gradients and thinner thermal boundary layers, indicating stronger thermal resistance.
- The shear-thinning behavior becomes more prominent as the viscosity ratio β increases (from 0.5 to 2.0), resulting in reduced effective viscosity and faster fluid motion.
- Graphical outcomes validate the accuracy of HPM in modeling cilia-driven Prandtl fluid flows, providing valuable insights for applications in biomedical systems (e.g., lungs and bile ducts) and porous geological media.

CRediT authorship contribution statement

Saira Muhammad Hussain: Writing – original draft, Resources, Methodology, Investigation. **Aqila Shaheen:** Writing – original draft, Investigation, Data curation, Conceptualization. **Ali Hasan Ali:** Writing – review & editing, Visualization, Supervision, Software, Project administration. **Ali Raza:** Writing – review & editing, Supervision, Formal analysis, Conceptualization. **Ahmed M. Abed:** Validation, Resources, Funding acquisition, Formal analysis.

Declaration of competing interest

The authors declare that they have no known competing financial interests or personal relationships that could have appeared to influence the work reported in this paper.

Acknowledgement

This study is supported via funding from Prince Sattam bin Abdulaziz University project number (PSAU/2024/R/1445).

Supplementary materials

Supplementary material associated with this article can be found, in the online version, at doi:10.1016/j.rineng.2025.105305.

Data availability

Data will be made available on request.

References

[1] C.H. Amanulla, S. Saleem, A. Wakif, M.M. Al-Qarni, MHD Prandtl fluid flow past an isothermal permeable sphere with slip effects, Case Stud. Therm. Eng. 14 (3) (2019) 100–447.
[2] M.I. Khan, S.A. Khan, T. Hayat, M.I. Khan, A. Alsaedi, Nanomaterial based flow of Prandtl–Eyring (non-Newtonian) fluid using brownian and thermophoretic diffusion with entropy generation, Comput. Methods Programs Biomed 180 (2) (2019) 105–107.
[3] J. Akram, N.S. Akbar, E. Maraj, Chemical reaction and heat source/sink effect on magnetonano Prandtl–Eyring fluid peristaltic propulsion in an inclined symmetric channel, Chin. J. Phys 65 (1) (2020) 300–313.
[4] I. Uddin, I. Ullah, R. Ali, I. Khan, K.S. Nisar, Numerical analysis of nonlinear mixed convective mhd chemically reacting flow of Prandtl–Eyring nanofluids in the presence of activation energy and joule heating, J. Therm. Anal. Calorim 145 (2) (2020) 495–505.
[5] I. Khan, A. Hussain, M.Y. Malik, S. Mukhtar, On magnetohydrodynamics Prandtl fluid flow in the presence of stratification and heat generation, Phys. Stat. Mech. Appl 540 (3) (2020) 123–128.
[6] H.A. Hussein, Numerical hydrothermal evaluation of heat transfer in a multi-mini-channel heat sink: effect of square pin fins, Results Eng. 20 (1) (2023) 101–403.
[7] A. Amador-Arjona, J. Elliott, A. Miller, A. Ginbey, G.J. Pazour, G. Enikolopov, A. V. Terskikh, Primary cilia regulate proliferation of amplifying progenitors in adult hippocampus: implications for learning and memory, J. Neurosci. 31 (2) (2011) 9933–9944.
[8] F.K. Bangs, N. Schrode, A.K. Hadjantonakis, K.V. Anderson, Lineage specificity of primary cilia in the mouse embryo, Nat. Cell Biol 17 (3) (2015) 113–122.
[9] N. Fatima, K.S. Nisar, S. Shaheen, M.B. Arain, N. Ijaz, T. Muhammad, A case study for heat and mass transfer of viscous fluid flow in double layer due to ciliated channel, Case Stud. Therm. Eng. 45 (2) (2023) 102–143.
[10] A. Shaheen, S. Nadeem, Metachronal wave analysis for non-Newtonian fluid inside a symmetrical channel with ciliated walls, Results phys. 7 (4) (2017) 1536–1549.
[11] K. Maqbool, S. Shaheen, A.M. Siddiqui, Effect of nano-particles on MHD flow of tangent hyperbolic fluid in a ciliated tube: an application to fallopian tube, Math. Biosci. Eng 16 (4) (2019) 2927–2941.
[12] S.N. Khaderi, M.G.H.M. Baltussen, P.D. Anderson, J.M.J. Den Toonder, P.R. Onck, Breaking of symmetry in microfluidic propulsion driven by artificial cilia, Phys. Rev. E 82 (2) (2010) 227–302.
[13] S. Akram, M. Athar, K. Saeed, A. Razia, M. Alghamdi, T. Muhammad, Impact of partial slip on double diffusion convection of sisko nanofluids in asymmetric channel with peristaltic propulsion and inclined magnetic field, Nanomaterials 12 (16) (2022) 27–36.
[14] A. Shaheen, M.I. Asjad, Peristaltic flow of a Sisko fluid over a convectively heated surface with viscous dissipation, J. Phys. Chem. Solids 122 (7) (2018) 210–217.
[15] S. Akram, et al., Convection theory on thermally radiative peristaltic flow of Prandtl tilted magneto nanofuid in an asymmetric channel with effects of partial slip and viscous dissipation, Mater. Today 35 (3) (2023) 106–111.
[16] O. Kazaz, R. Ferraro, M. Tassieri, S. Kumar, G. Falcone, N. Karimi, M.C. Paul, Sensible heat thermal energy storage performance of mono and blended nanofluids in a free convective-radiation inclined system, Case Stud. Therm. Eng. 51 (4) (2023) 103–142.
[17] O. Kazaz, N. Karimi, M.C. Paul, Radiation and nanoparticle interaction for enhanced light absorption and heat conversion, J Mol Liq 411 (4) (2024) 125–137.
[18] Z. Ullah, A. Abbas, E.R. El-Zahar, L.F. Seddek, A. Akgul, A.M. Hassan, Significance of thermal density and viscous dissipation on heat and mass transfer of chemically reactive nanofluid flow along stretching sheet under magnetic field, Results Eng. 20 (3) (2023) 101–413.

[19] Z. Jia, Y. Xuan, Analysis on interaction among solar light and suspended nanoparticles in nanofluids, J. Quant. Spectrosc. Radiat. Transf 269 (3) (2021) 107–692.
[20] S. Bhattacharyya, N. Jain, T. Bhatt, H. Yasmin, M. Sharifpur, Mini-channel cooling system for solar PV panels with hybrid magnetic nanofluid and magnetic field, Results Eng. 20 (2) (2023) 101–473.
[21] M.A. Imran, A. Shaheen, E.S.M. Sherif, M. Rahimi-Gorji, A.H. Seikh, Analysis of peristaltic flow of Jeffrey six constant nano fluid in a vertical non-uniform tube, Chin. J. Phys. 66 (1) (2020) 60–73.
[22] A. Shaheen, S. Nadeem, Metachronal wave analysis for non-Newtonian fluid inside a symmetrical channel with ciliated walls, Results phys. 7 (4) (2017) 1536–1549.
[23] S.U. Jan, U. Khan, M. Abd El-Rahman, S. Islam, A.M. Hassan, A. Ullah, Effect of variable thermal conductivity of ternary hybrid nanofluids over a stretching sheet with convective boundary conditions and magnetic field, Results Eng. 20 (3) (2023) 101–531.
[24] O. Kazaz, N. Karimi, S. Kumar, G. Falcone, M.C. Paul, Effects of combined radiation and forced convection on a directly capturing solar energy system, Therm. Sci. Eng. Prog. 40 (3) (2023) 101–127.
[25] O. Kazaz, E. Abu-Nada, Thermal performance of nano-architected phase change energetic materials for a next-generation solar harvesting system, Energy Convers. Manag. 32 (7) (2025) 119–141.
[26] T. Hayat, M.I. Khan, M. Tamoor, M. Waqas, A. Alsaedi, Numerical simulation of heat transfer in MHD stagnation point flow of cross fluid model towards a stretched surface, Results Phys 7 (2) (2017) 1824–1827.
[27] M.A. Abdelhafez, A.M. Abd-Alla, S.M. Abo-Dahab, Y. Elmhedy, Influence of an inclined magnetic field and heat and mass transfer on the peristaltic flow of blood in an asymmetric channel, Sci Rep 13 (2) (2023) 5749–5775.
[28] M. Jawad, Z. Shah, S. Islam, W. Khan, A.Z. Khan, Nanofluid thin film flow of Sisko fluid and variable heat transfer over an unsteady stretching surface with external magnetic field, J Algorithm Comput Technol 13 (2) (2019) 174–198.
[29] S. Saleem, M.M. Al-Qarni, S. Nadeem, N. Sandeep, Convective heat and mass transfer in magneto jeffrey fluid flow on a rotating cone with heat source and chemical reaction, Commun Theor Phys 70 (5) (2018) 534–627.
[30] A. Raza, O.V. Stadoleanu, A.M. Abed, A.H. Ali, M. Sallah, Heat transfer model analysis of fractional Jeffery-type hybrid nanofluid dripping through a poured microchannel, Int. J. Thermofluids 22 (2024) 100656.
[31] A. Shaheen, M.I. Asjad, S. Arshad, Three dimensional flow of nanofluids over an exponential horizontal nonlinear sheet saturated in porous medium, J. homepage 37 (2) (2019) 555–561.
[32] S. Akram, K. Saeed, M. Athar, A. Riaz, A. Razia, M.A. Al-Malki, Interaction of induced magnetic field, double diffusion convection and multiple slips for thermal radiative biological flow of six-constant Jeffreys nanofluid: advancements in mechanics, Sep Sci Technol 60 (2) (2025) 316–339.
[33] M. Amir, Q. Ali, A. Raza, M.Y. Almusawa, W. Hamali, A.H. Ali, Computational results of convective heat transfer for fractionalized Brinkman type tri-hybrid nanofluid with ramped temperature and non-local kernel, Ain Shams Eng. J. 15 (3) (2024) 102576.
[34] L.A. Carter, J.L. MacDonald, A.J. Roskams, Olfactory horizontal basal cells demonstrate a conserved multipotent progenitor phenotype, J Neurosci 24 (2) (2004) 5670–5683.
[35] A. Raza, O.V. Stadoleanu, A.M. Abed, A.H. Ali, M. Sallah, Heat transfer model analysis of fractional Jeffery-type hybrid nanofluid dripping through a poured microchannel, Int. J. Thermofluids 22 (2024) 100656.
[36] C.H. Amanulla, A. Wakif, Z. Boulahia, M.S. Reddy, N. Nagendra, Numerical investigations on magnetic field modeling for Carreau non-newtonian fluid flow past an isothermal sphere, J. Braz. Soc. Mech. Sci. Eng 40 (9) (2018) 1–15.
[37] A. Raza, R. Ali, S.M. Eldin, S.H. Alfalqui, A.H. Ali, New fractional approach for CMC and water based hybrid nanofluid with slip boundary layer: applications of fractal fractional derivative, Case Stud. Therm. Eng. 49 (2023) 103280.
[38] K. Zheng, A. Raza, A.M. Abed, H. Khursheed, L.F. Seddek, A.H. Ali, A.U. Haq, New fractional approach for the simulation of (Ag) and (TiO2) mixed hybrid nanofluid flowing through a channel: fractal fractional derivative, Case Stud. Therm. Eng. 45 (2023) 102948.